Optimal Measurement Location Planning for Localizing Underwater Transponders

Jesse Garcia, Jay A. Farrell, and Zaher M. Kassas
Department of Electrical and Computer Engineering
University of California, Riverside
Riverside, California 92507
{jegarcia, farrell}@ece.ucr.edu , and zkassas@ieee.org

***Abstract*—An autonomous surface vehicle optimally plans acoustic measurement locations to localize a set of pre-deployed underwater transponders (UTs). Once localized, these transponders could serve as reference beacons for underwater navigation. An optimal measurement location planning (OMLP) strategy, in the D-optimality sense, is developed to localize this set of UTs. It is shown that the matrix optimization criterion corresponding to the D-optimality criterion simplifies to a scalar optimization problem for single UT environments. Simulation results are presented demonstrating the computational benefit of this simplification over the standard D-optimality criterion. Experimental results are given illustrating the proposed OMLP strategy to localize one and two unknown UTs to within a few meters.**

I. Introduction

Global navigation satellite system (GNSS) signals become severely attenuated underwater, rendering them unusable at depths below a few feet. Inertial navigation systems (INS) are prevalent in underwater navigation. To correct drift inherent in INS, underwater vehicles typically utilize a network of pre-deployed underwater transponders (UTs), surface vehicles, or resurfacing strategies. Resurfacing is not desirable in situations where stealth and covertness are required. Also, it wastes valuable resources, such as time and energy. This paper focuses on localizing a set of randomly pre-deployed UTs at unknown locations. Once the UT locations are known, they could serve as reference beacons for underwater navigation.

This paper considers the following problem. An autonomous surface vehicle (ASV) is estimating the positions (i.e., localizing) a number of UTs that are rigidly attached to the sea floor. Where should the ASV place itself to optimally localize the UTs? This problem is analogous to optimal sensor placement, to which many optimization criteria have been developed.

Among the most common optimization criteria is the D-optimality, namely maximization of the logarithm of the determinant of the Fisher information matrix [1]. The D-optimality criterion yields the maximum reduction in target location uncertainty as measured by the volume of the uncertainty ellipsoid [2], [3]. An alternative, computationally efficient optimization criterion based on innovation maximization was proposed in [4], which was shown to be identical to the D-optimality criterion under linear Gaussian assumptions and was demonstrated to yield comparable performance with non-linear pseudorange measurements. Another computationally efficient criterion with a geometric interpretation for sensor placement based on pseudorange measurements was proposed in [5]. Such criterion was shown to yield a family of convex optimization problems that could be solved in parallel. A collaborative sensor placement strategy was developed in [6], wherein a network of coordinated ASVs attempt to optimally place themselves to localize a single UT.

While the above papers considered planar sensor placement, a three-dimensional (3D) sensor placement strategy is needed for certain underwater and aerial applications. In underwater applications, an additional complexity arises from the fact that once submerged, an underwater vehicle is deprived of GNSS signals; hence, accurate positioning information about itself. This forces a reliance on onboard inertial sensor suites that provide rapidly decaying self-positioning estimates due to integral effects. Aided navigation and simultaneous localization and mapping (SLAM) techniques can be used to mitigate this decay. In [7], inertial sensor drift was calibrated using lower rate sensors (e.g., magnetic, transponders, and pressure). Other approaches to this problem for underwater scenarios were developed in [8] for sonar-based terrain-aided navigation (TAN). In [9], criteria were developed to ensure observability of the nonlinear system when ranging to a single acoustic beacon, while [10] derives such criteria when measuring pseudoranges to multiple terrestrial signal transmitters.

This paper develops an optimal measurement location planning (OMLP) strategy for an ASV in an environment comprising multiple randomly pre-deployed UTs, each at an unknown location. The ASV makes acoustic range measurements to the UTs, computes an estimate of the location of the UTs along with the estimation error covariance, and plans the D-optimal measurement location to which it should move next.

The remainder of this paper is organized as follows. Section II formulates the UT and OMLP problems. Section III presents a maximum *a posteriori* (MAP) approach to solve the UT localization problem and a computationally efficient approach to solve the OMLP problem. Section IV presents simulation results demonstrating both solutions. Section V presents experimental results showing OMLP for one and two UTs with a localization accuracy of a few meters. Concluding remarks are given in Section VI.

This work was supported in part by the Office of Naval Research (ONR) under Grant N00014-16-1-2768.

978-1-5386-1647-5/18/$31.00 ©2018 IEEE

II. UT Localization and OMLP Problem Formulation

This section formulates the UT localization and OMLP problems. The UT localization begins after three measurements have been made, according to the method presented in Section III-A. The OMLP strategy is computed after each localization computation, according to the method presented in Section III-B.

Throughout this paper, $\boldsymbol{p}_T^m \in \mathbb{R}^3$ denotes the 3-D position of the m^{th} UT, where $m = 1, \cdots, M$, with M being the total number of UTs; while $\boldsymbol{p}_V(n) \in \mathbb{R}^3$ denotes the position of the ASV at the n^{th} measurement epoch. The set of all ASV locations is denoted by ${}^N\mathcal{P}_V = \{\boldsymbol{p}_V(1), \cdots \boldsymbol{p}_V(N)\}$. The ASV positions are assumed to be known (e.g., from GNSS signals). An estimate of $\boldsymbol{p}_T^m$ based on N range measurements is denoted by ${}^N\hat{\boldsymbol{p}}_T^m$.

The true range between the m^{th} UT and the ASV at the n^{th} epoch is

$$r^m(n) = ||\boldsymbol{p}_T^m - \boldsymbol{p}_V(n)||_2. \tag{1}$$

This range measurement is modeled as

$$z^m(n) = r^m(n) + w^m(n), \tag{2}$$

where $w^m(n)$ is the measurement noise, which is assumed to be independent and identically distributed with $w^m(n) \sim \mathcal{N}(0, \sigma^2)$. The vector of range measurements to the m^{th} UT is denoted by

$$\boldsymbol{z}^m = \boldsymbol{r}^m + \boldsymbol{w}^m \in \mathbb{R}^{N\times 1}, \tag{3}$$

where $\boldsymbol{r}^m \triangleq [r^m(1), \cdots, r^m(N)]^\mathsf{T}$ is the vector of true range measurements and $\boldsymbol{w}^m \triangleq [w^m(1), \cdots, w^m(N)]^\mathsf{T}$ is the corresponding vector of measurement noise samples. The range can be estimated by substituting ${}^N\hat{\boldsymbol{p}}_T^m$ into (1)

$$\hat{r}^m(n) = ||{}^N\hat{\boldsymbol{p}}_T^m - \boldsymbol{p}_V(n)||_2. \tag{4}$$

The vector of estimated ranges is

$$\hat{\boldsymbol{r}}^m = [\hat{r}^m(1), \cdots, \hat{r}^m(N)]^\mathsf{T} \in \mathbb{R}^{N\times 1}. \tag{5}$$

The Jacobian vector $\boldsymbol{h}^m(n) = \dfrac{\partial}{\partial \boldsymbol{p}_T^m(N)} [\hat{r}^m(n)]$ is

$$\boldsymbol{h}^m(n) = \frac{\left[{}^N\hat{\boldsymbol{p}}_T^m - \boldsymbol{p}_V(n)\right]^\mathsf{T}}{\hat{r}^m(n)} \in \mathbb{R}^{1\times 3}. \tag{6}$$

For all measurement epochs $n = 1, \cdots, N$, the vectors in (6) are stacked into the matrix

$$\mathbf{H}^m = \left[(\boldsymbol{h}^m(1))^\mathsf{T}, \cdots, (\boldsymbol{h}^m(N))^\mathsf{T}\right]^\mathsf{T} \in \mathbb{R}^{N\times 3}. \tag{7}$$

Problem 1: UT Localization

Given $\boldsymbol{z}^m$ and ${}^N\mathcal{P}_V$, estimate ${}^N\boldsymbol{p}_T^m$.

Problem 2: OMLP: M ≥ 1

For M UTs in the environment, given $\{{}^N\hat{\boldsymbol{p}}_T^m\}_{m=1}^M$, select $\boldsymbol{p}_V(N+1)$ that will minimize the aggregate uncertainty of the next estimates ${}^{N+1}\hat{\boldsymbol{p}}_T^m$ for $m = 1, \cdots, M$.

III. Solution to the UT Localization and OMLP Problems

This section presents solutions to the UT localization and OMLP problems. To reduce the linearization error on UT localization, an iterative Gauss-Newton approach is adopted [11] along with a MAP estimation formulation. The iterative estimation algorithm is initialized with an estimate and corresponding covariance, denoted by ${}_0\hat{\boldsymbol{p}}_T^m$ and ${}_0\mathbf{P}_T^m$, respectively.

A. *Solution 1: UT localization*

Let the pre-subscript j denote the iteration number. For example, the estimate of $\boldsymbol{p}_T^m$ at the j^{th} iteration is ${}_j\hat{\boldsymbol{p}}_T^m$. Estimated ranges and Jacobians at the j^{th} iteration, ${}_j\hat{r}^m(n)$ and ${}_j\mathbf{h}^m(n)$, are computed by substituting ${}_j\hat{\boldsymbol{p}}_T^m$ into (4) and (6). Similarly, ${}_j\hat{\boldsymbol{r}}^m$ and ${}_j\mathbf{H}^m$ are constructed by substituting ${}_j\hat{r}^m(n)$ and ${}_j\mathbf{h}^m(n)$, $\forall n \le N$, into (5) and (7).

A MAP framework is adopted. The basic optimization problem is

$${}^N\hat{\boldsymbol{p}}_T^m = \underset{\boldsymbol{p}_T^m}{\operatorname{argmax}} \left[p(\boldsymbol{z}^m|\boldsymbol{p}_T^m)\, p(\boldsymbol{p}_T^m)\right]. \tag{8}$$

The assumption $\boldsymbol{p}_T^m \sim \mathcal{N}({}_0\hat{\boldsymbol{p}}_T^m, {}_0\mathbf{P}_T^m)$ with a very large ${}_0\mathbf{P}_T^m$ implies having virtually no prior information about $\boldsymbol{p}_T^m(N)$. With $w(n)$ in (2) assumed to be zero-mean Gaussian, the distribution of the measurement is $\boldsymbol{z}^m \sim \mathcal{N}(\boldsymbol{r}^m, \mathbf{R})$, where $\mathbf{R} = \sigma^2\, \mathbf{I}_{3\times 3}$.

Defining the composite vectors $\boldsymbol{y} = \left[(\boldsymbol{z}^m)^\mathsf{T}, ({}_0\hat{\boldsymbol{p}}_T^m)^\mathsf{T}\right]^\mathsf{T}$ and $\boldsymbol{v}(\boldsymbol{p}_T^m) = \left[(\boldsymbol{r}^m)^\mathsf{T}, (\boldsymbol{p}_T^m)^\mathsf{T}\right]^\mathsf{T}$ and the covariance matrix for $\boldsymbol{y}$, $\mathbf{C}^{-1} = \text{blkdiag}\left[\mathbf{R}^{-1}, ({}_0\mathbf{P}_T^m)^{-1}\right]$, the objective function of (8) is equivalent to

$$\mathcal{J}_{MAP}(\boldsymbol{p}_T^m) = \frac{-1}{2} \left[\boldsymbol{y} - \boldsymbol{v}(\boldsymbol{p}_T^m)\right]^\mathsf{T} \mathbf{C}^{-1} \left[\boldsymbol{y} - \boldsymbol{v}(\boldsymbol{p}_T^m)\right], \tag{9}$$

where $\text{blkdiag}(\cdot)$ denotes the block-diagonal matrix. This allows (8) to be rewritten as

$${}^N\hat{\boldsymbol{p}}_T^m = \underset{\boldsymbol{p}_T^m}{\operatorname{argmin}} \quad \mathcal{J}_{MAP}(\boldsymbol{p}_T^m). \tag{10}$$

The MAP estimate of $\boldsymbol{p}_T^m$ is computed by solving the batch nonlinear least-squares optimization problem in (10) iteratively. Let j be the iteration counter, starting with $j = 0$. Let the j^{th} estimate of $\boldsymbol{p}_T^m$ be ${}_j\hat{\boldsymbol{p}}_T^m$. The estimated range vector is ${}_j\hat{\boldsymbol{r}}^m = \hat{\boldsymbol{r}}^m|_{\hat{\boldsymbol{p}}_T^m = {}_j\hat{\boldsymbol{p}}_T^m}$. The vector $\boldsymbol{v}(\boldsymbol{p}_T^m)$ is linearized around ${}_j\hat{\boldsymbol{p}}_T^m$ at each iteration, yielding

$$\boldsymbol{v}(\boldsymbol{p}_T^m) \approx \boldsymbol{v}({}_j\hat{\boldsymbol{p}}_T^m) + \mathbf{V}_j\, \delta\boldsymbol{p}_j, \tag{11}$$

where

$$\mathbf{V}_j = \begin{bmatrix} \mathbf{H}^m({}_j\hat{\boldsymbol{p}}_T^m) \\ [1,\ 0,\ 0] \\ [0,\ 1,\ 0] \\ [0,\ 0,\ 1] \end{bmatrix} \in \mathbb{R}^{(N+3)\times 3}, \tag{12}$$

$$\delta\boldsymbol{p}_j = \boldsymbol{p}_T^m - {}_j\hat{\boldsymbol{p}}_T^m. \tag{13}$$

Define $\delta\boldsymbol{y}_j = \boldsymbol{y} - \boldsymbol{v}({}_j\hat{\boldsymbol{p}}_T^m)$. The MAP objective function in (10) is the same as

$$\mathcal{J}_{MAP}(\delta\boldsymbol{p}_j) = (\delta\boldsymbol{y}_j - \mathbf{V}_j\, \delta\boldsymbol{p}_j)^\mathsf{T} \mathbf{C}^{-1} (\delta\boldsymbol{y}_j - \mathbf{V}_j\, \delta\boldsymbol{p}_j). \tag{14}$$

The linearized objective function (14) is minimized when

$$\delta \boldsymbol{p}_j \;=\; (\mathbf{V}_j^{\mathsf{T}}\mathbf{C}^{-1}\mathbf{V}_j)^{-1}\mathbf{V}_j^{\mathsf{T}}\mathbf{C}^{-1}\delta \boldsymbol{y}_j. \tag{15}$$

A new estimate is computed as

$$_{j+1}\hat{\boldsymbol{p}}_T^m = {}_j\hat{\boldsymbol{p}}_T^m \;+\; \delta \boldsymbol{p}_j. \tag{16}$$

Iterations continue until $||_{j+1}\hat{\boldsymbol{p}}_T^m \;-\; {}_j\hat{\boldsymbol{p}}_T^m||_2 \;\leq\; \delta_{min}$ as long as $j \;\leq\; J_{max}$, for user-defined J_{max} and δ_{min}. After convergence, the covariance is computed as

$${}^N\mathbf{P}_T^m \;=\; (\mathbf{V}_j^{\mathsf{T}}\mathbf{C}^{-1}\mathbf{V}_j)^{-1}. \tag{17}$$

B. *Solution 2: OMLP*

The D-optimality criterion [12, p. 387] is used to determine $\boldsymbol{p}_V(N+1)$ that will maximize the information gain. For this section, the subscript N corresponds to the number of ASV locations. The symbol $\mathbf{Y}_N^m \in \mathbb{R}^{3\times 3}$ denotes the information matrix after n ASV measurements to the m^{th} UT (i.e., $\mathbf{Y}_N^m = ({}^N\mathbf{P}_T^m)^{-1}$).

Define $\mathbf{D}_N^m(\boldsymbol{x}) \;=\; \mathbf{h}^m(N)^{\mathsf{T}}\,\mathbf{h}^m(N)$, where the symbol $\boldsymbol{x} = \boldsymbol{p}_V(N+1)$ is used to simplify notation and $\mathbf{h}^m(N)$ depends on $\boldsymbol{p}_V(N+1)$. When the $(N+1)$-st range measurement is made, the information matrix becomes

$$\mathbf{Y}_{N+1}^m(\boldsymbol{x}) \;=\; \sigma^{-2}\,\mathbf{D}_{N+1}^m(\boldsymbol{x}) + \mathbf{Y}_N^m. \tag{18}$$

Define $\mathbf{Y}_{N+1} = \text{diag}(\mathbf{Y}_{N+1}^1, \ldots, \mathbf{Y}_{N+1}^M)$.

D-optimality is used to determine the ASV's next measuring location in an environment with M UTs. The D-optimality optimization problem is

$$\begin{aligned} \boldsymbol{x}^* \;&= \underset{\boldsymbol{x}}{\text{argmax}} \quad \mathcal{J}(\boldsymbol{x}) \\ &\quad\;\; \text{subject to} \quad g(\boldsymbol{x}) \leq\; d_{max}, \end{aligned} \tag{19}$$

where

$$\mathcal{J}(\boldsymbol{x}) \;=\; \log\det\left[\mathbf{Y}_{N+1}(\boldsymbol{x})\right] \tag{20}$$

$$g(\boldsymbol{x}) \;=\; \|\boldsymbol{x} \;-\; \boldsymbol{p}_V(N)|_2^2 \tag{21}$$

The boundary constraint $g(\boldsymbol{x}) \leq d_{max}$ restricts the maximum distance to which the ASV could travel to make the next measurement.

Given the form of (18) and the fact that each $\mathbf{Y}_N^m$ is independent of $\boldsymbol{x}$, (19) reduces to

$$\begin{aligned} \boldsymbol{x}^* \;&= \underset{\boldsymbol{x}}{\text{argmax}} \quad \log f(\boldsymbol{x}) \\ &\quad\;\; \text{subject to} \quad g(\boldsymbol{x}) \leq\; d_{max}, \end{aligned} \tag{22}$$

where $f(\boldsymbol{x}) \;=\; \prod_{m=1}^M \det\left[\mathbf{Y}_{N+1}^m(\boldsymbol{x})\right]$. Using the properties of the logarithm function,

$$\log f(\boldsymbol{x}) = \sum_{m=1}^{M} \log\det\left[\mathbf{Y}_{N+1}^m(\boldsymbol{x})\right]. \tag{23}$$

Sylvester's matrix determinant theorem [13] could be applied to (23) to give

$$\begin{aligned} \det\left[\mathbf{Y}_{N+1}^m(\boldsymbol{x})\right] \;&=\; \det[\mathbf{Y}_N^m]\cdot \\ &\det[1 + (\boldsymbol{h}^m(N+1))(\mathbf{Y}_N^m)^{-1}\,(\boldsymbol{h}^m(N+1))^{\mathsf{T}}]. \end{aligned} \tag{24}$$

Define

$$\alpha^m(\boldsymbol{x}) \;=\; [\boldsymbol{h}^m(N+1)](\mathbf{Y}_N^m)^{-1}\,[\boldsymbol{h}^m(N+1)]^{\mathsf{T}}, \tag{25}$$

which is a positive scalar. Using (24)-(25), the optimization function in (23) can be simplified to

$$\log f(\boldsymbol{x}) = \sum_{m=1}^{M} \log[(1+\alpha^m(\boldsymbol{x}))\det[\mathbf{Y}_N^m]]. \tag{26}$$

Properties of the logarithm function allow further simplification to

$$\log \mathbf{A}(\boldsymbol{x}) = \sum_{m=1}^{M} \log(1+\alpha^m(\boldsymbol{x})) \;+\; \sum_{m=1}^{M} \log\det[\mathbf{Y}_N^m]. \tag{27}$$

The term $\sum_{m=1}^M \log\det[\mathbf{Y}_N^m]$ is constant with respect to $\boldsymbol{x}$, so it can be dropped.

Letting $\bar{\mathcal{J}}(\boldsymbol{x}) = \sum_{m=1}^M \log(1+\alpha^m(\boldsymbol{x}))$, the optimization problem of (22) is written as

$$\begin{aligned} \boldsymbol{x}^* \;&= \underset{\boldsymbol{x}}{\text{argmax}} \quad \bar{\mathcal{J}}(\boldsymbol{x}) \\ &\quad\;\; \text{subject to} \quad g(\boldsymbol{x}) \leq\; d_{max}. \end{aligned} \tag{28}$$

Note that for $M \;=\; 1$, (28) is the same as

$$\begin{aligned} \boldsymbol{x}^* \;&= \underset{\boldsymbol{x}}{\text{argmax}} \quad \bar{\mathcal{J}}'(\boldsymbol{x}) \\ &\quad\;\; \text{subject to} \quad g(\boldsymbol{x}) \leq\; d_{max}, \end{aligned} \tag{29}$$

where $\bar{\mathcal{J}}'(\boldsymbol{x}) \;=\; \alpha(\boldsymbol{x})$.

IV. Simulation Results

This section presents simulation results for the UT localization and OMLP problems.

A. *Gauss-Newton MAP estimator for UT localization*

The Gauss-Newton MAP estimator treats each UT independently. Therefore, this section considers the single UT case (the superscript $m \;=\; 1$ is dropped). A Monte Carlo type analysis is performed, simulating 500 runs of the MAP estimation algorithm. For each run, four measurements are used to estimate $\boldsymbol{p}_T$. The ASV makes $N = 4$ measurements from the locations listed in Table I.

TABLE I
ASV locations used in Monte Carlo analysis

Symbol	Value (m)
$\boldsymbol{p}_V(1)$	$[\;\;5\,,\;\;\;0\,,\;0]^{\mathsf{T}}$
$\boldsymbol{p}_V(2)$	$[\;\;0\,,\;\;\;5\,,\;0]^{\mathsf{T}}$
$\boldsymbol{p}_V(3)$	$[-5\,,\;\;\;0\,,\;0]^{\mathsf{T}}$
$\boldsymbol{p}_V(4)$	$[\;\;0\,,\;-5\,,\;0]^{\mathsf{T}}$

The UT is fixed at $\boldsymbol{p}_T = [-2, -7, -7]^\mathsf{T}$. The value ${}_0\hat{\boldsymbol{p}}_T$ is drawn from a zero-mean Gaussian distribution with covariance ${}_0\mathbf{P}_T = \text{diag}[100, 100, 4]$. The USBL measurement noise standard deviation $\sigma = 0.1$ m corresponds to the SeaTrac x150 USBL product sheet [14].

Fig. 1 compares the 95% confidence ellipse in the $x - y$ plane from (17) to that fitted to 500 samples of $\hat{\boldsymbol{p}}_T^m$. The match can be seen to be very good.

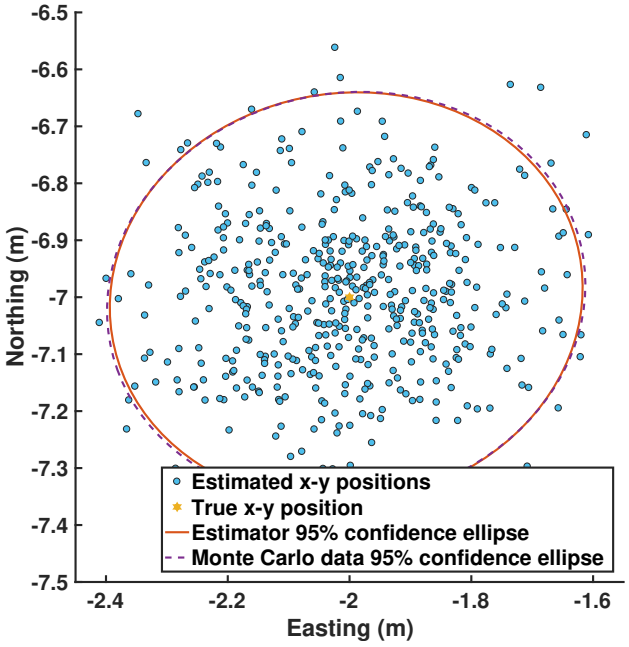

Fig. 1. Scatter plot of $\hat{\boldsymbol{p}}_T$ in the $x - y$ plane. The solid ellipse is created by fitting the 500 samples of $\hat{\boldsymbol{p}}_T(4)$ and displays the true uncertainty in the estimate. The dashed ellipse is created using $\mathbf{P}_T$ from (17) and represents the 95% confidence ellipse calculated from the Monte Carlo data. The ellipses are comparable, suggesting the estimator is performing correctly.

B. Evaluation of OMLP for M = 1

This section evaluates the OMLP strategy for the single UT case (the superscript m is dropped). The optimization problems outlined in (29) and (19) are solved numerically in MATLAB using the function fmincon. The UT is again placed at $\boldsymbol{p}_T = [-2, -7, -7]^\mathsf{T}$. The initial assumed location of UT_1 is ${}_0\hat{\boldsymbol{p}}_T = [-10.10, -17.95, -9.65]^\mathsf{T}$ with covariance ${}_0\mathbf{P}_T = \text{diag}[100, 100, 4]$. As before, the measurement noise standard deviation is set to $\sigma = 0.1$m.

It is worth noting that the solution to the unconstrained maximization of (25) is achieved when $\boldsymbol{h}^m(N+1)$ lies along the eigenvector associated with the largest eigenvalue of $\mathbf{Y}_N$. This in turn yields a $\boldsymbol{p}_V(N+1)$ along this eigenvector. As d_{max} decreases, the motion constraint comes into play, such that $\boldsymbol{p}_V(N+1)$ may not be able to lay along this eigenvector.

Using $\boldsymbol{p}_V(1) = [0, 0, 0]^\mathsf{T}$ as the first measurement location, Fig. 2 demonstrates this aspect of the path planner by plotting $\boldsymbol{p}_V(2)$ planned according to (29) as a function of d_{max} using a sequence of green diamonds. Given one measurement, $\hat{\boldsymbol{p}}_T(1)$ is shown as a purple dot. Its error ellipse is shown in solid purple and the direction of its largest eigenvector is shown as a dashed purple arrow. When d_{max} is small, $\boldsymbol{p}_V(2)$ is constrained to be near $\boldsymbol{p}_V(1)$. As d_{max} increases, $\boldsymbol{p}_V(2)$ moves away from $\boldsymbol{p}_V(1)$ and towards the ray defined by the eigenvector.[1] The blue solid and yellow dashed circles display the boundary of the feasible region when $d_{max} = 10$m and $d_{max} = 30$m respectively. The value of $\boldsymbol{p}_V(2)$ for $d_{max} = 10$m is marked by a blue asterisk and the value of $\boldsymbol{p}_V(2)$ for $d_{max} = 30$m is marked by a yellow asterisk. Note that the solutions are on the boundary of the feasible set.

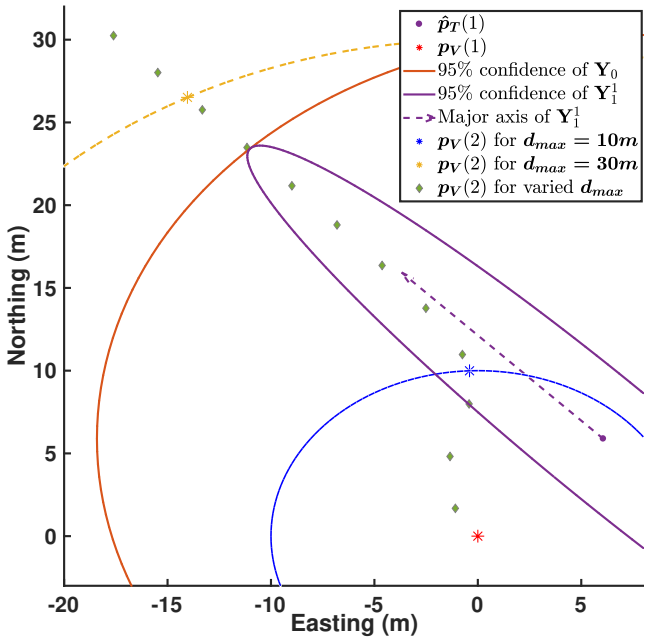

Fig. 2. The green sequence of diamonds indicates the optimal solution $\boldsymbol{p}_T(2)$ as function of d_{max}. A red asterisk denotes $\boldsymbol{p}_V(1)$. The 95% confidence ellipse corresponding to $\mathbf{Y}_0$ is shown in dark red, whereas that of $\mathbf{Y}_1$ is shown in dark purple. The largest eigenvector of $\mathbf{Y}_1^1$ corresponds to the dashed purple arrow pointing in the direction of the major axis of the purple ellipse.

C. Evaluation of OMLP for M = 4

This subsection evaluates the OMLP for the case where $M = 4$, using $N_p = 12$ vehicle positions. The motion constraint uses $d_{max} = 10$m. The true UT locations and initial location estimates are provided in Table II. Using the prior for the UT positions, the initial ASV position is determined according to (28) to be $\boldsymbol{p}_V(1) = [-9.78, 2.10, 0]^\mathsf{T}$.

Each initial uncertainty was set to ${}_0\mathbf{P}_T^m = \text{diag}[50, 50, 4]$. Fig. 3 displays snapshots of the environment at measurement epochs 2 and 3. Final localization results corresponding to this scenario are provided in Table III. The first row of Table III shows the norm of the error between the the true UT location and the final estimated location (i.e., $||\tilde{\boldsymbol{p}}_T^m||_2 = ||\boldsymbol{p}_T^m - {}^{N_p}\hat{\boldsymbol{p}}_T^m||_2$) and subsequent rows show standard deviations in the final estimation error (i.e., $\sigma_i = \sqrt{{}^{N_p}\mathbf{P}_T^m(i,i)}, i = 1, 2, 3$) in

[1]Two solutions are possible for this simple example, depending on whether the vehicle moves to the northwest or to the southeast. For this example, we always choose the solution to the northwest.

millimeters. Columns of this table organize this data for each UT.

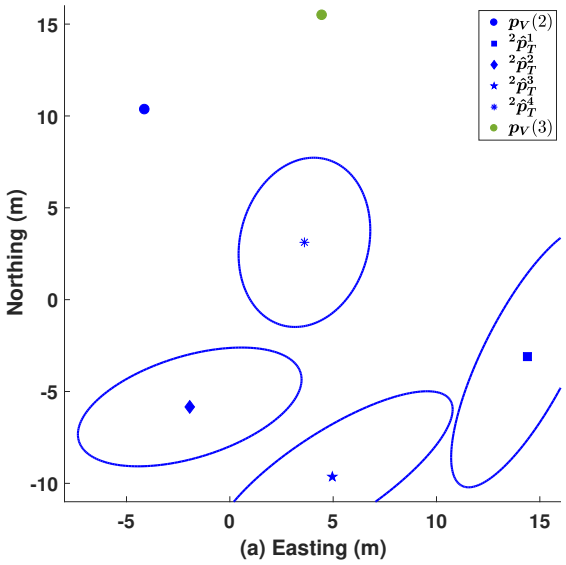

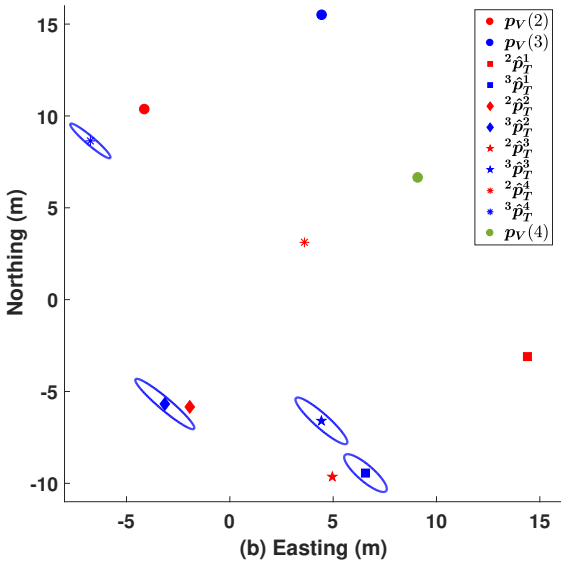

Fig. 3. (a) Environment at measurement epoch $n = 2$. (b) Environment at measurement epoch $n = 3$. In (a) and (b), all symbols drawn in blue represent items relevant to the epoch that is the input to the OMLP algorithm. Green symbols denotes immediate future values (i.e., OMLP outputs). Red symbols denotes immediate past values. Circles represent vehicle locations. Squares, diamonds, stars, and asterisks correspond to $\hat{\boldsymbol{p}}_T^i(n)$ for all $1 \leq i \leq 4$. The 95% confidence ellipses associated with $\mathbf{Y}_n^i$ are drawn as blue ellipses around the current UT estimates.

TABLE II
SIMULATION SETTING OF OMLP FOR $M = 4$

Symbol	Value (m)
$\boldsymbol{p}_T^1$	$[\ 6, -9, -8]^\mathsf{T}$
$\boldsymbol{p}_T^2$	$[-3, -6, -6]^\mathsf{T}$
$\boldsymbol{p}_T^3$	$[\ 4, -6, -8]^\mathsf{T}$
$\boldsymbol{p}_T^4$	$[-7,\ \ 9, -7]^\mathsf{T}$
${}_0\hat{\boldsymbol{p}}_T^1$	$[\ 14.40, -3.10, -5.74]^\mathsf{T}$
${}_0\hat{\boldsymbol{p}}_T^2$	$[\ -1.94, -5.84, -5.19]^\mathsf{T}$
${}_0\hat{\boldsymbol{p}}_T^3$	$[\ \ 4.96, -9.64, -6.02]^\mathsf{T}$
${}_0\hat{\boldsymbol{p}}_T^4$	$[\ \ 3.61,\ \ 3.12, -5.46]^\mathsf{T}$
σ	0.1

TABLE III
LOCALIZATION RESULTS FROM FIG. 3 USING OMLP

Value (mm)	$\boldsymbol{p}_T^1$	$\boldsymbol{p}_T^2$	$\boldsymbol{p}_T^3$	$\boldsymbol{p}_T^4$
$\|\|\tilde{\boldsymbol{p}}_T\|\|_2$	81	95	123	55
σ_x	46	41	44	43
σ_y	56	49	54	55
σ_z	72	78	65	74

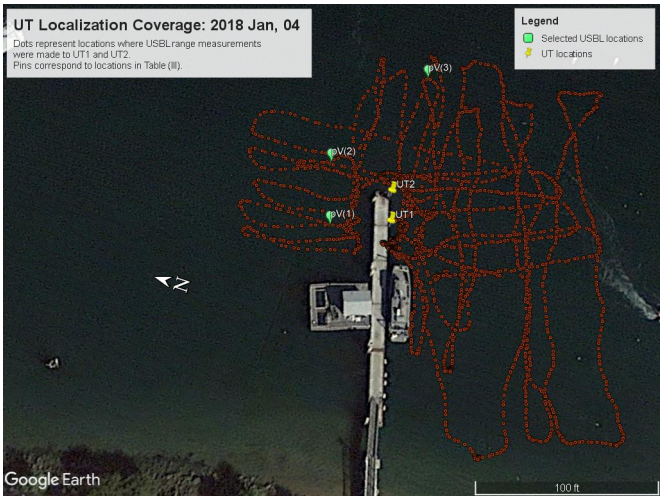

Fig. 4. Top-down view of the the testing area and acoustic ranging locations as measured by the Hemisphere GPS compass. Yellow push-pin markers display the configuration of UTs during data collection. Green tear-drop markers denote the three measuring locations used in Section IV for localization of UT1.

V. EXPERIMENTAL RESULTS

A. Data collection

Data collection for both single and multiple transponder environments occurred on January 4^{th}, 2018 along pier 169 at SPAWAR SSC Pacific, San Diego, California, USA. Fig. 4 illustrates the testing environment. Two SeaTrac x010 acoustic beacons acted as UTs and were fixed to the pier at a depth of 1m.

A manned surface craft equipped with a SeaTrac x150 USBL beacon and Hemisphere v104s satellite-based augmentation system (SBAS) GPS compass maneuvered in the ocean near the pier while ranging to each UT. The GPS computed differential GPS (DGPS) position estimates, which were accu-

rate to 1m. Range data and GPS fixes were acquired at 0.67Hz and 1Hz, respectively, and were written to two separate files during collection. All data was time-stamped with UTC time, which was used to align data in post-processing. Ground truth positions of these UTs were determined by averaging GPS fixes at each UT mounting point over periods of 3 minutes.

The range measurement standard deviation was estimated using sets of approximately 250 range measurements. Ground truth ranges were determined from GPS position fixes to be $r_1 = 9.22$m and $r_2 = 2.67$m. Fig. 5 presents range and measurement noise standard deviation estimates using maximum likelihood:

$$\begin{bmatrix} \hat{r}_i \\ \hat{\sigma}_i \end{bmatrix} = \begin{bmatrix} \frac{1}{i}\sum_{n=1}^{i} r(n) \\ \sqrt{\frac{1}{i-1}\sum_{n=1}^{i}\left[r(n)-\hat{R}(n)\right]^2} \end{bmatrix}. \quad (30)$$

In Fig. 5(a)-(b), the final value $\hat{r}_1 = 9.02$m and $\hat{r}_2, = 2.66$m are displayed as solid red lines. The estimated range after the i-th measurement is shown as a red crosses. The solid blue curves show the the final value of the range plus and minus estimated standard deviation in the estimated range after measurement i. In Fig. 5(c), both the final value of $\hat{\sigma}_1 = 62$mm and $\hat{\sigma}_2 = 113$mm are displayed as solid red lines. The values of $\hat{\sigma}_1$ and $\hat{\sigma}_2$ after the i-th measurement are displayed as red and blue markers, respectively. Solid blue curves represent the final values of $\hat{\sigma}_1$ and $\hat{\sigma}_2$ plus and minus the estimates of their standard deviation.

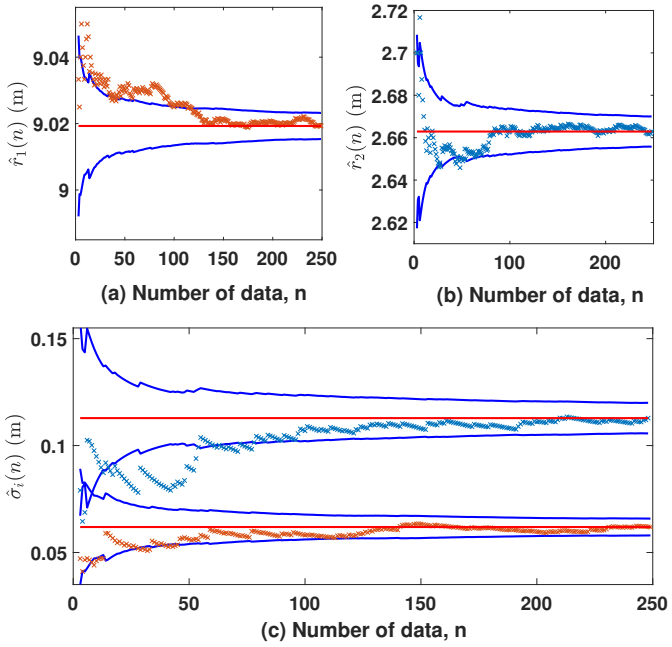

Fig. 5. (a),(b) The estimated range between the USBL and each of the two transponders using (30). (c) The estimated range standard deviation.

Note that $\hat{\sigma}_1$ and $\hat{\sigma}_2$ differ by approximately 50mm. The difference in $\hat{\sigma}_i$ suggests that measurement noise varies with distance. The maximum of both standard deviation estimates was used as the standard deviation of all measurements for the MAP estimation algorithm, i.e., $\sigma = \max\{\hat{\sigma}_i\} = 113$mm. Also, $\hat{r}_1$ differs from the ground truth value by approximately 0.2 meters, which may be explained by the uncertainty associated with the GPS measurements.

B. Processed Results: Localization

TABLE IV
CONSTANTS USED FOR SINGLE TRANSPONDER LOCALIZATION OF UT_1

Symbol	Value (m)
$\boldsymbol{p}_V(1)$	$[33.87\,,\ 25.42\,,\ -22.14]^\mathsf{T}$
$\boldsymbol{p}_V(2)$	$[28.47\,,\ \ 2.10\,,\ -51.60]^\mathsf{T}$
$\boldsymbol{p}_V(3)$	$[50.18\,,\ \ 7.16\,,\ -32.37]^\mathsf{T}$
σ	0.12

In this subsection, all symbols are presented in the ECEF coordinate frame. Table IV contains constants used in validating the MAP estimation algorithm. All positions in Table IV are in a local ECEF frame, determined by translating the global ECEF frame by $[-2.448 \times 10^6\,,\ -4.7559 \times 10^6\,,\ 3.4117 \times 10^6]$. These positions are labeled in Fig. 4. A set of 3 range and GPS measurements (i.e. $N_p = 3$) were selected and used in the MAP estimation algorithm. The value of $\boldsymbol{p}_T^1 = [32.79\,,\ 9.96\,,\ -39.53]^\mathsf{T}$m was measured via GPS for comparison. The MAP estimation algorithm was initialized with ${}_0\hat{\boldsymbol{p}}_T^1 = [27.35\,,\ 13.25\,,\ -41.32]^\mathsf{T}$m and ${}_0\mathbf{P}_T^1 = \text{diag}[100, 100, 4]\text{m}^2$.

The final localization results are provided in Table V. The rows of this table provide the final estimated UT location ${}^{N_p}\hat{\boldsymbol{p}}_T^1$, the norm of the error (i.e., $||\tilde{\boldsymbol{p}}_T^1||_2 = ||\boldsymbol{p}_T^1 - {}^{N_p}\hat{\boldsymbol{p}}_T^1||_2$), and the theoretical standard deviation of the final estimate (i.e., $\sigma_i = \sqrt{{}^{N_p}\mathbf{P}_T^1(i,i)}$, $i = 1, 2, 3$).

TABLE V
LOCALIZATION RESULTS OF UT_1

Symbol	Value (m)
${}^3\hat{\boldsymbol{p}}_T^1$	$[32.80\,,\ 10.45\,,\ -41.09]^\mathsf{T}$
$\|\|\tilde{\boldsymbol{p}}_T^1\|\|_2$	1.63
$\{\sigma_x^1,\ \sigma_y^1,\ \sigma_z^1\}$	$\{1.17,\ 2.05,\ 1.84\}$

C. Processed Results: Localization: OMLP with $M = 1$

In this subsection, the symbol $\boldsymbol{x} = \boldsymbol{p}_V(N+1)$ is used to simplify notation. The optimal next measurement location $\boldsymbol{x}^*$ computed by fmincon could not be in the set of available ASV locations $\mathcal{P}_V$. Therefore, the point used for the next range measurement $\bar{\boldsymbol{x}}$ was chosen from $\mathcal{P}_V$ according to

$$\bar{\boldsymbol{x}} = \underset{\boldsymbol{x}\in\mathcal{P}_V}{\text{argmin}} \quad ||\boldsymbol{x} - \boldsymbol{x}^*||_2. \quad (31)$$

OMLP was performed starting after the third measurement for 3 more measurements ($N_p = 6$). The motion constraint d_{max} was set to 10m. Table VI contains final results of this experiment. The rows of this table provide measurement locations $\boldsymbol{p}_V(n)$ for $4 \leq n \leq N_p$ in the local ECEF frame, the final estimated UT location ${}^{N_p}\hat{\boldsymbol{p}}_T^1$, the norm of the error (i.e., $||\tilde{\boldsymbol{p}}_T^1||_2 = ||\boldsymbol{p}_T^1 - {}^{N_p}\hat{\boldsymbol{p}}_T^1||_2$), and the theoretical standard deviations in the final estimate (i.e. $\sigma_i = \sqrt{{}^{N_p}\mathbf{P}_T^1(i,i)}, i = 1,2,3$). Note that the theoretical accuracy is decreasing with the number of range measurements and is much smaller than the computed accuracy $||\tilde{\boldsymbol{p}}_T^1||_2$. The most likely reason is that the GPS measurement of the UT position is not correct due to either GPS errors or the challenge of placing the GPS receiver directly above the underwater UT.

TABLE VI
LOCALIZATION RESULTS OF UT_1 WITH OMLP

Symbol	Value (m)
$\boldsymbol{p}_V(4)$	$[51.66, -3.34, -46.01]^\mathsf{T}$
$\boldsymbol{p}_V(5)$	$[49.61, -5.85, -52.50]^\mathsf{T}$
$\boldsymbol{p}_V(6)$	$[45.08, -7.40, -58.06]^\mathsf{T}$
${}^{N_p}\hat{\boldsymbol{p}}_T^1$	$[31.88, \quad 8.65, -39.47]^\mathsf{T}$
$\|\|\tilde{\boldsymbol{p}}_T^1\|\|_2$	1.60
$\{\sigma_x^1, \sigma_y^1, \sigma_z^1\}$	$\{0.11, 0.25, 0.20\}$

D. Processed Results: Localization: OMLP with $M = 2$

The OMLP was applied to a multi-UT scenario using $N_p = 12$ measurements. The true UT location $\boldsymbol{p}_V(1) = [22.09, 9.25, -37.94]^\mathsf{T}$ is determined by evaluating (28). As before, d_{max} was set to 10m. The final localization results and select measurement locations are provided in Table VII. The results in this table are organized similarly to those in table VI. The same comments discussed in Subsection V-C apply regarding the final error $||\tilde{\boldsymbol{p}}_T^m||_2$ being larger than the theoretical standard deviation σ_i^m.

TABLE VII
LOCALIZATION RESULTS OF UT_1 AND UT_2 WITH OMLP

Symbol	Value (m)
$\boldsymbol{p}_V(1)$	$[\ 22.09, \ \ 9.25, -37.94]^\mathsf{T}$
$\boldsymbol{p}_V(6)$	$[\ 23.98, 13.04, -41.35]^\mathsf{T}$
$\boldsymbol{p}_V(12)$	$[\ 25.10, 14.33, -43.36]^\mathsf{T}$
${}^{12}\hat{\boldsymbol{p}}_T^1$	$[\ 30.96, 11.83, -37.33]^\mathsf{T}$
${}^{12}\hat{\boldsymbol{p}}_T^2$	$[\ 24.70, 12.87, -40.60]^\mathsf{T}$
$\|\|\tilde{\boldsymbol{p}}_T^1\|\|_2$	3.43
$\|\|\tilde{\boldsymbol{p}}_T^2\|\|_2$	2.77
$\{\sigma_x^1, \sigma_y^1, \sigma_z^1\}$	$\{0.33, 0.60, 0.50\}$
$\{\sigma_x^2, \sigma_y^2, \sigma_z^2\}$	$\{0.13, 0.18, 0.16\}$

VI. CONCLUSIONS AND DISCUSSIONS

This article provided a MAP estimation algorithm for localizing underwater transponders as well as a theoretical foundation for determining future best acoustic ranging locations of an ASV. The simulation results demonstrated the performance of the proposed estimator and measurement location planning strategy. The experimental results based on data collected at SPAWAR SSC Pacific demonstrated the performance of the OMLP strategy in an environment containing two UTs. Future work will aim at reducing effects of unmodeled errors (e.g., variable noise standard deviation with distance and position uncertainty from GPS).

ACKNOWLEDGMENTS

The authors would like to thank Joe Khalife and Elahe Aghapour for helpful discussions. The authors are also grateful to the unmanned marine vehicles (UMV) lab at SPAWAR SSC Pacific for help with data collection.

REFERENCES

[1] D. Uciński, *Optimal Measurement Methods for Distributed Parameter System Identification*. CRC Press, 2005.

[2] D. Salinas-Moreno, N. Crasta, M. Ribiero, B. Bayat, A. Pascoal, and J. Aranda, "Integrated motion planning, control, and estimation for range-based vehicle positioning and target localization," *in Proceedings of IFAC Conference on Control Applications in Marine Systems*, vol. 49, no. 23, pp. 34 – 40, September 2016.

[3] Z. Kassas and T. Humphreys, "Motion planning for optimal information gathering in opportunistic navigation systems," *in Proceedings of AIAA Guidance, Navigation, and Control Conference*, pp. 4551 – 4565, August 2013.

[4] Z. Kassas, T. Humphreys, and A. Arapostathis, "Greedy motion planning for simultaneous signal landscape mapping and receiver localization," *IEEE Journal of Selected Topics in Signal Processing*, vol. 9, pp. 246 – 258, March 2015.

[5] J. Morales and Z. Kassas, "Optimal collaborative mapping of terrestrial transmitters: receiver placement and performance characterization," *IEEE Transactions on Aerospace and Electronic Systems*, vol. 54, no. 2, pp. 992–1007, April 2018.

[6] B. Ferriera, A. Matos, H. Campos, and N. Cruz, "Localization of a sound source: optimal positioning of sensors carried on autonomous surface vehicles," *in Proceedings of IEEE Marine Technological Society OCEANS*, pp. 1 – 8, September 2013.

[7] P. Miller, J. Farrell, Y. Zhao, and V. Djapic, "Autonomous underwater vehicle navigation," *IEEE Journal of Oceanic Engineering*, vol. 35, no. 3, pp. 663–678, July 2010.

[8] F. Teixeira, J. Quintas, and A. Pascoal, "AUV terrain-aided doppler navigation using complementary filtering," *in Proceedings of IFAC Conference on Maneuvering and Control of Marine Craft*, vol. 45, pp. 313 – 318, September 2012.

[9] P. Batista, C. Silvestre, and P. Oliveira, "Single range aided navigation and source localization: Observability and filter design," *Systems & Control Letters*, vol. 60, no. 8, pp. 665 – 673, June 2011.

[10] Z. Kassas and T. Humphreys, "Receding horizon trajectory optimization in opportunistic navigation environments," *IEEE Transactions on Aerospace and Electronic Systems*, vol. 51, no. 2, pp. 866–877, April 2015.

[11] Y. Bar-Shalom, T. Kirubarajan, and X.-R. Li, *Estimation with Applications to Tracking and Navigation*. John Wiley & Sons, Inc., 2002.

[12] S. Boyd and L. Vanderbuerghe, *Convex Optimization*. Cambridge University Press, 2004.

[13] M. Brookes. The matrix reference manual. [Online]. Available: http://www.ee.ic.ac.uk/hp/staff/dmb/matrix/proof003.html#DetBlock_p

[14] *SeaTrac Micro-USBL Tracking and Data Modems*, Blueprint Design Engineering Ltd, March 2016, rev. 5.